5th Joint International Symposium on Deformation Monitoring (JISDM), 20-22 June 2022, Valencia, Spain
DOI: http://doi.org/10.4995/JISDM2022.2022.13620

Bridge deformations during train passage: monitoring multiple profiles using concurrently operating MIMO-SAR sensors

Andreas Baumann-Ouyang[1], Jemil Avers Butt[1, 2], Andreas Wieser[1]

[1] Institute of Geodesy and Photogrammetry, ETH Zürich, Stefano-Franscini-Platz 5, 8093 Zurich, Switzerland, (andreas.baumann@geod.baug.ethz.ch; jemil.butt@geod.baug.ethz.ch; andreas.wieser@geod.baug.ethz.ch)
[2] Atlas optimization GmbH, Zürich, Switzerland, (jemil.butt@atlasoptimization.ch)

Key words: *synthetic aperture radar (SAR); structural health monitoring (SHM); bridge monitoring; deformation; vibration*

ABSTRACT

Sensors capable of measuring surface deformations with areal coverage and high spatial and temporal resolution are beneficial for many monitoring applications. However, such sensors are typically expensive, or their configuration cannot be adapted flexibly by the user like in case of satellite-based systems. Automotive Multiple-Input-Multiple-Output Synthetic Aperture Radar (MIMO-SAR) systems are interesting potential alternatives associated with low cost and high flexibility. In this paper, we present an experimental investigation showing the capabilities of a particular off-the-shelf, automotive radar system for structural monitoring. We analyse the accuracy of the measured line-of-sight displacements, the spatial and temporal resolution, and the impact of simultaneous coverage of the same area by two sensors of the same type. Finally, we demonstrate the MIMO-SAR system in a real-world use case measuring deformations of a railway bridge in response to dynamic load by trains passing over it. We operated two MIMO-SAR sensors simultaneously, analyse and interpret the individual interferograms and combine the data to derive the temporal and spatial distribution of vertical displacements along selected profiles. The results show that off-the-shelf automotive-grade MIMO-SAR systems can be used to quantify sub-millimetre deformations of structures and derive high-resolution time series beneficial for structural health monitoring applications.

I. Introduction

A. *Overview*

Many natural and artificial structures are monitored to mitigate the risk of failure or fatal events, e.g. landslides (Chae *et al.*, 2017), dams (Scaioni *et al.*, 2018), or bridges (Enckell, 2011; Lienhart *et al.*, 2017, Galmarini *et al.*, 2020). A large variety of sensors with different strengths and weaknesses is being applied for deformation monitoring. Radar sensors are particularly attractive because of their areal coverage, the high sensitivity with respect to deformations, and their capability to provide useful signals in a large range of weather conditions. Terrestrial radar interferometry (TRI) can measure surface deformations with sub-millimetre precision and a temporal resolution on the level of milliseconds (Rödelsperger, 2011; Caduff *et al.*, 2015; Baumann-Ouyang *et al.*, 2021). It is therefore a technology with potential applications in structural health monitoring (SHM) as changes of the frequency response of a structure over time can be used to identify and locate potential damage (Sampaio *et al.*, 1999, Holst *et al.*, 2020). As of now, the actual application of TRI in this field is mainly limited to scientific investigations. This could change with a special type of low-cost radar systems: Multiple Input Multiple Output Synthetic Aperture Radar (MIMO-SAR) systems. These systems are currently developed particularly for automotive applications and allow quantifying line-of-sight (LOS) displacements with 2D spatial resolution over a wide field of view (almost 180°), with high data rate (>100 Hz) and with very high precision (µm-level standard deviations) despite the low-cost.

MIMO-SAR systems employing frequency modulated continuous waves (FMCW) have thus been applied already for monitoring bridges (Miccinesi *et al.*, 2021; Pieraccini *et al.*, 2019; Tian *et al.*, 2019) and buildings (D'Aria *et al.*, 2019). In each of these applications, only one MIMO-SAR system at a time was used. Due to the low cost, it is also feasible to operate several MIMO-SAR systems simultaneously and covering the same object from different viewing angles. This allows (i) improving the spatial coverage, e.g. by acquiring multiple profiles, and (ii) improving the information content by deriving displacement vectors in an external coordinate frame rather than LOS displacements only. However, using FMCW radar systems with the same or similar frequencies may cause interference and degrade the resulting observations (Amar *et al.*, 2021).

In this work, we investigate the influence of using equal or different frequencies when operating two MIMO-SAR systems simultaneously with overlapping spatial coverage. We then deploy the MIMO-SAR systems for monitoring a railway bridge and derive the vertical displacements caused by trains passing over it.

BY-NC-SA 2022, Editorial Universitat Politècnica de València

We first review the principles of MIMO-SAR, then introduce the experimental devices in Section II. In Section III we investigate interference, and in Section IV we describe and analyse the bridge monitoring experiment. We conclude in Section V.

B. *Principles of MIMO-SAR*

Terrestrial radar interferometry is a measurement technique used in combination with FMCW radar systems (Rödelsperger, 2011). A transmitting antenna (TXA) emits an electromagnetic wave that is reflected within illuminated scene and subsequently registered by a receiving antenna (RXA). Range resolution is a consequence of the bandwidth of the signal, angular resolution is either achieved by large rotating antennas (real aperture radar, RAR) or by small antennas radiating and receiving at different positions (synthetic aperture radar, SAR). MIMO-SAR implements the latter principle using multiple TXA and RXA in a fixed assembly.

Each pair of TXA and RXA creates one virtual antenna (VA). The TXA and RXA can be positioned in such a way that all resulting VA are arranged linearly and regularly separated, representing a uniform linear array (ULA). For such a system, we define a 3D cartesian coordinate system with its X^R-axis along the ULA, the Y^R-axis parallel to the antenna boresight direction, and the Z^R-axis complementing a right-handed system (Figure 1). The position of a scatter S_i in this coordinate systems can also be expressed in polar coordinates with:

- range R_i i.e., distance between the centre of the ULA and S_i,
- azimuth θ_i i.e., deflection from boresight in the X^RY^R-plane; and
- elevation ε_i i.e., deflection from X^RY^R-plane.

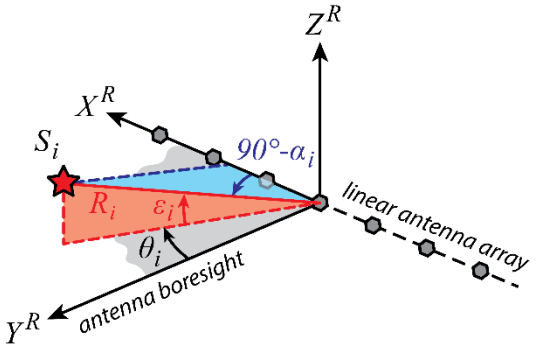

Figure 1. Definition coordinate system and angles (see text) of a MIMO-SAR system with linear antenna array.

Azimuth and elevation are commonly used to indicate angles within or from a horizontal plane. For simplicity we still use these terms herein although the X^RY^R-plane of a MIMO-SAR sensor does not have to be horizontal and thus, in this paper, azimuth and elevation do not refer to the gravity field of the Earth.

The radar instrument is not sensitive to azimuth and elevation but instead yields the range R_i and the cross-range angle α_i which is the angle between the Y^RZ^R-plane and the line-of-sight to S_i. For scatterers close to the X^RY^R-plane, however, cross-range and azimuth are approximately equal.

The result of one measurement is the phase ϕ. The outcome of one full radar acquisition is a single look complex image (SLC) *i.e.*, a complex-valued matrix whose dimension corresponds to the number of resolution cells in range and cross-range. The complex numbers represent the amplitude and phase of the radar signal scattered back by the surfaces at the location corresponding to the respective range and cross-range. The amplitude encodes the total power scattered back to the radar instrument from the corresponding surfaces. The phase is related to the range R of the scatterer and the wavelength λ of the signal as (Eq. 1):

$$\phi = \frac{(2 \cdot \pi) \cdot (2 \cdot R)}{\lambda} (\mathrm{mod}\ 2\pi) \tag{1}$$

The core idea of TRI is to calculate the line-of-sight (LOS) displacement ΔD_{LOS} of the respective surfaces between two epochs t_1 and t_2 from the phase measurements obtained at those epochs (Eq. 2):

$$\Delta D_{LOS} = \left(\phi_{t_1} - \phi_{t_2}\right) \cdot \frac{\lambda}{4\pi} \tag{2}$$

Depending on the instrument's configuration and data rate, this allows measuring displacements at high temporal and spatial resolution. Displacements as small as a few µm can be detected. Displacements larger than $\lambda/4$ are ambiguous due to Equation 1 but can still be recovered by phase unwrapping (*e.g.*, Yu *et al.*, 2019).

The actual displacement will typically not occur in the LOS direction. However, if the direction of displacement in relation to the radar's coordinate system is known from other sources, or if LOS measurements are made simultaneously with instruments from different locations, the LOS displacement, Equation 2, can be transformed into the actual displacement. We use the former approach in Section IV where we set up radar sensors below the bridge with the antenna array parallel to a vertical plane through the longitudinal axis of the bridge, and the antenna boresight inclined by an angle υ above the horizon. The situation is indicated in Figure 2.

The relation between vertical displacement ΔU_i and LOS displacement ΔD_{LOS_i} can be derived directly from the figure in this case (Eq. 3):

$$\Delta U_i = \Delta D_{LOS_i} \cdot \sin(\upsilon + \alpha_i) \tag{3}$$

2022, Editorial Universitat Politècnica de València BY-NC-SA

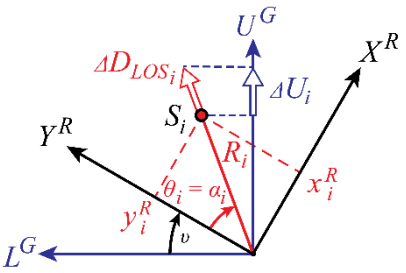

Figure 2. Relation of vertical displacement ΔU_i and the MIMO-SAR system's LOS displacement ΔD_{LOS_i} for a specific setup of the radar instrument and a scatterer within the instrument's $X^R Y^R$-plane (U^G indicates the up-direction in the local gravity field, and L^G the longitudinal axis in the horizontal plane).

II. Experimental Device

A. *Characteristics of the experimental Device*

For our experimental investigations, we use two Texas Instruments TIDEP-01012 (Rev. E) MIMO-SAR systems (see Figure 3). Each of these devices has 12 transmitting and 16 receiving antennas arranged such as to yield $N = 86$ virtual antennas spaced by λ/2 in a ULA where λ denotes the average wavelength. The instrument's frequency range is 77 to 81 GHz, limiting the configurable bandwidth Δf to a maximum of 4 GHz. This implies a range and cross-range resolution of (Eqs. 3 and 4):

$$\Delta r = \frac{c}{2 \cdot \Delta f} \geq 3.75 \text{ cm} \tag{4}$$

$$\Delta\theta = \frac{2}{N \cdot \cos(\theta_k)} = \frac{1.33 \text{ deg}}{\cos(\theta)} \tag{5}$$

respectively, see (Baumann-Ouyang *et al.*, 2021) and (Rao, 2018) for details. In the configuration used herein, the systems cannot distinguish different elevations but rather integrate the signals from all scatterers within ± 20 deg elevation (corresponding to the antenna beam width) into the SLC bin corresponding to the respective azimuth and cross-range. We have so far used the system with acquisition rates of up to 400 Hz, *i.e.* obtaining up to 400 SLCs per second. Due to memory and communication bandwidth constraints the evaluation boards used herein do not allow arbitrarily long continuous data acquisition but require a break of a few seconds for data transfer after a maximum of 65'535 SLCs.

B. *Accuracy*

In Baumann-Ouyang *et al.* (2021), we showed that the accuracy and the range of application of the TIDEP are affected by noise and biases. In previous investigations, we observed an empirical standard deviation of approximately 7 µm for a time series of deformations associated to a single pixel at a distance of 20 m from the instrument and sampled at 400 Hz. Temperature variations of the onboard chips introduce scale-factor variations of approximately 10 ppm in the initial warm-up phase. On a longer timescale, the uncertainty of the phase observations is dominated by meteorological changes—especially changes in humidity and temperature. A change of temperature by +2°C or of relative humidity of +4%, not accounted for, creates the same phase change as an actual deformation of around 50 µm at a distance of 20 m and under standard atmospheric conditions, as can be verified using the equations given by Rüeger (2002).

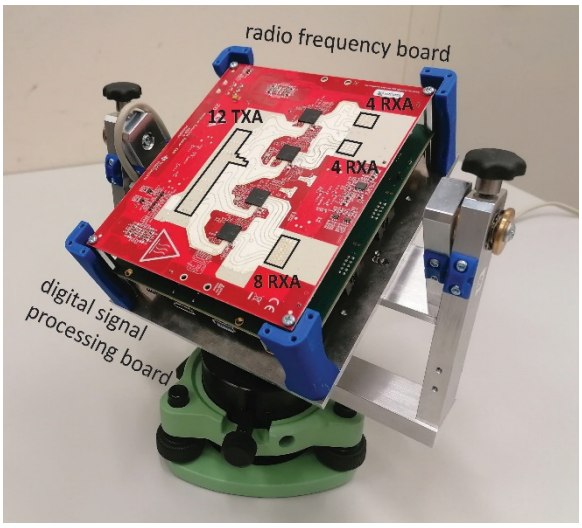

Figure 3. TIDEP-01012 (digital signal processing board, and radio frequency board with 12 TXA and 16 RXA) on custom made holder for mounting during experiments.

C. *Chirp Configuration*

The TIDEP-01012 MIMO-SAR system supports a wide range of chirp configurations when operated via the native Texas Instruments mmWave Studio software and Lua scripting. For the following investigations, we used two different configurations, see Table 1, which result in a range resolution of 10 cm with a maximum unambiguous distance of 51 m.

Table 1. Chirp, timing, and analogue/digital conversion (ADC) parameters for the experiments

Parameter configuration		
	F1	F2
Centre Frequency f_c [GHz]	77.95	79.95
Sweep Bandwidth Δf [MHz]	1498.5	
Frequency Slope s_c [MHz/µs]	65.854	
Idle Time T_{Idle} [µs]	3	
ADC Starting Time $T_{ADC,Start}$ [µs]	3	
Ramp Duration T_{Ramp} [µs]	28	
Frame Duration T_{Frame} [µs]	372	
Samples per Chirp N_{ADC} [-]	512	
ADC Sampling Frequency f_{ADC} [MHz]	22.5	

Figure 4a shows a typical FMCW chirp and some of the parameters. The acquisition of an entire scene requires to consecutively emit a chirp from every TXA (Figure 4b-c) which takes a time of T_{Frame}. A subsequent acquisition can be started after a short

BY-NC-SA 2022, Editorial Universitat Politècnica de València

break of $T_{InterFrame}$. This break is required because of the limited onboard storage rate and needs to last between 0.3 and 1342 ms (Texas Instruments, 2020).

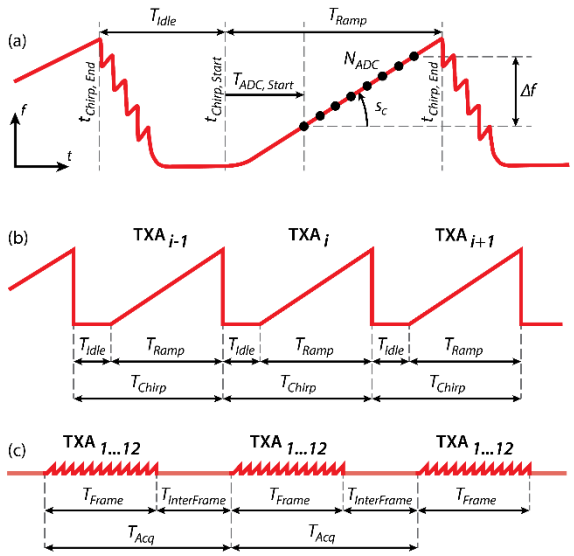

Figure 4. FMCW acquisition with associated chirp and timing parameters: (a) typical FMCW chirp; (b) simplified chirps for a series of consecutively emitting TXA; and (c) frame structure to acquire an entire dataset. Adapted from (Dham, 2020).

III. Experimental Investigation of Interference

A. *Interference*

Using two or more sensors simultaneously allows to observe different parts of a larger structure at the same time. However, the presence of multiple radar sensors with uncoordinated transmissions at the same frequencies is known to impact the measurements negatively (Amar *et al.*, 2021) because of unwanted interference. This results from signals of one instrument being received by another instrument and mixing with that instrument's own signals. A future solution to avoid unwanted interference could be based on time synchronisation of all the devices, *e.g.* by triggering the sensors with a common timing signal like a GNSS pulse per second or a dedicated controller. With only one sensor active at a time, the available frequency bands would be used optimally. However, there is currently no synchronization solution available for the given MIMO-SAR systems. One option to avoid interference in this case is to use non-overlapping frequency bands (like configurations F1 and F2 in Table 1) which deteriorates the attainable range resolution, see Equation 4, as compared to using the whole bandwidth. An alternative is to accept the presence of interference but pseudo-randomize its temporal appearance by providing inter-frame periods much larger than the frame durations (see Figure 4) and using slightly different inter-frame periods for the different devices. In this way, the chirps emitted by the different devices will overlap only at some times and thus cause interference during short periods while not overlapping at others. The likelihood of interferences could be further reduced by using narrower bandwidth or steeper frequency slopes and by (further) increasing the inter-frame periods at the cost of temporal and spatial resolution. While this pseudo-randomizing approach is only useful for applications where the times with interference can be detected from the results and filtering out those times does not impair the benefit of the measurement system, we will use this approach herein for the opposite purpose, i.e. to assure that we actually do have interference at some times.

B. *Experimental setup*

In Baumann-Ouyang *et al.* (2021), we showed that the TIDEP-01012 MIMO-SAR system can reliably detect movements of a corner cube by as few as 25 µm in an indoor environment. We repeated the experiment in a 23 m long hallway with relatively stable atmospheric conditions to investigate the influence of two radar sensors concurrently emitting signals, herein.

The two instruments were set up next to each other facing along the hallway. A corner cube with an edge length of 40 mm was mounted on a motorised translation stage located at a distance of roughly 19 m, see Figure 5, and moved over a total distance of 2.5 mm in steps of 25 µm, remaining stable for two seconds at each location. The experiment was carried out twice, using the same configuration (F1, see Table 1) of both radar instruments once, i.e., overlapping frequencies, and different configuration (F1, F2), i.e., non-overlapping frequencies, the other time.

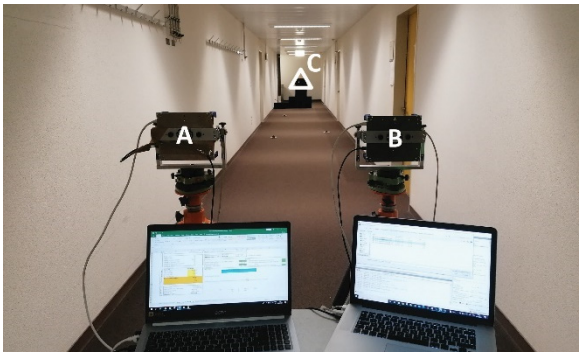

Figure 5. Measurement setup for the indoor experiment. A and B indicate the two TIDEP-01012 devices and C denotes the corner cube.

We cannot choose $T_{InterFrame}$ short enough to assure close to 100% temporal overlap between the chirps of the two devices and using the same acquisition rate T_{Acq} for both devices would lead to a constant but unknown chirp overlap and thus amount of interference. So, we chose acquisition rates T_{Acq} = 1250 µs and T_{Acq} = 1251 µs for the two devices, respectively. This results in a complete overlap of the chirps every 1.25 s and at least a partial overlap for approximately 60% of the time, thus enabling us to investigate the effect of interference.

2022, Editorial Universitat Politècnica de València BY-NC-SA

C. *Results and analysis*

We formed interferograms and derived the cumulative displacements representing the motion of the corner cube mounted on the translation stage. Figure 6 shows excerpts of the resulting time series for device A and for times with overlapping (top) and non-overlapping frequencies (bottom) of the two, simultaneously operating devices. The RMSE of these observations are approximately 6.4 µm when the frequencies overlap and 5.7 µm when they do not. Both values are comparable to the empirical standard deviation of 7 µm based on earlier experiments (see Section II). Similar results are also obtained for other parts of the scene monitored during these experiments: Figure 7 shows the calculated displacements for a bin representing a rough plastered wall *i.e.*, a stable diffusive natural reflector instead of a moving corner cube. The RMSE values for these observations are 6.5 µm and 5.5 µm, respectively. Since the interference varies over time it does not show up strongly in the RMSE values, but it is visually recognizable by the distinct peaks in Figures. 6 (top) and 7 (top).

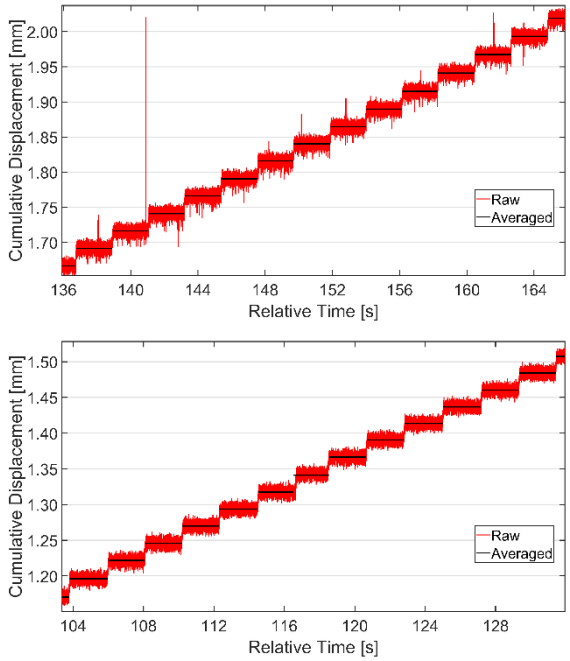

Figure 6. Cumulative displacement measurement observed by instrument A for one bin representing a corner cube for the acquisition setup with overlapping (top) and non-overlapping frequencies (bottom).

Based on this analysis, we can confirm that overlapping frequencies cause interference leading to corrupted measurements. However, with the devices used herein the impact is surprisingly small, may be reduced by filtering the displacement time series, and may even be negligible for many applications. We leave it for future work to study the interference more comprehensively and clarify whether there are circumstances where the impacts are much larger or would possibly even affect phase-unwrapping. However, if the resulting reduced bandwidths are sufficient, it is advisable to avoid overlapping frequencies and instead use disjoint sets of frequency ranges when operating two or more radar instruments simultaneously.

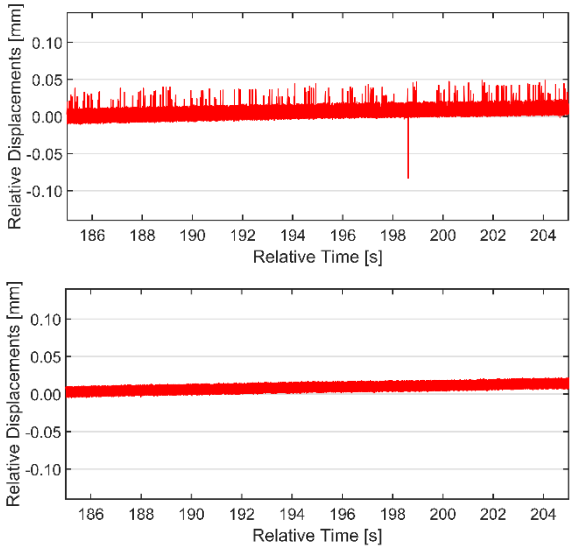

Figure 7. Cumulative displacement measurement observed by instrument A for one bin representing an area on the wall at the end of the floor for the acquisition setup with overlapping (top) and non-overlapping frequencies (bottom). In both cases, a trend caused by warm-up (Baumann-Ouyang *et al.*, 2021) is visible.

IV. Experimental Monitoring Application

A. *Experimental setup*

We selected a twin-track, prestressed concrete train bridge as an object for monitoring using MIMO-SAR sensors. The bridge is subject to short-term deformations at the sub-mm level with trains passing on top. Two radar instruments (A, B) were mounted on tripods below the bridge, see Figures 8 and 9. They were set up with their antenna array in a vertical plane along the bridge and the antenna boresight tilted upward with an elevation of approximately 45° *i.e.*, using a geometric configuration as depicted in Figure 2. The acquisition rate was set to 100 Hz and the other parameters were set for non-overlapping frequencies according to the values in Table 1.

Figure 8. Situation during the bridge monitoring experiment where A and B indicate the two TIDEP-01012 devices, P1-P3 selected areas on the upper soffit, MP and TS a metallic platform and a tram shelter, respectively.

BY-NC-SA 2022, Editorial Universitat Politècnica de València

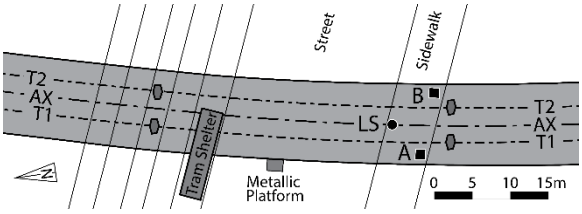

Figure 9. Map of the measurement setup for the bridge monitoring experiment where A and B indicate the locations of the two TIDEP-01012 devices, LS the location of a laser scanner, T1 and T2 the axes of the train tracks and AX the symmetry axis.

B. *Initial observations and processing*

An exemplary amplitude image can be seen in Figure 10 (top). It shows the typical distribution of amplitudes for the acquisition geometry sketched in Figure 8. Metallic constructions like the tram shelter or the metallic platform on the bridge, with appropriate orientation relative to the radar instruments, produce high amplitude signal returns. Also some other surfaces yield strong signal returns, with the strongest ones being found for surfaces illuminated almost orthogonally (*i.e.*, line-of-sight perpendicular to the surface) and for surfaces locally representing corner cube like shapes.

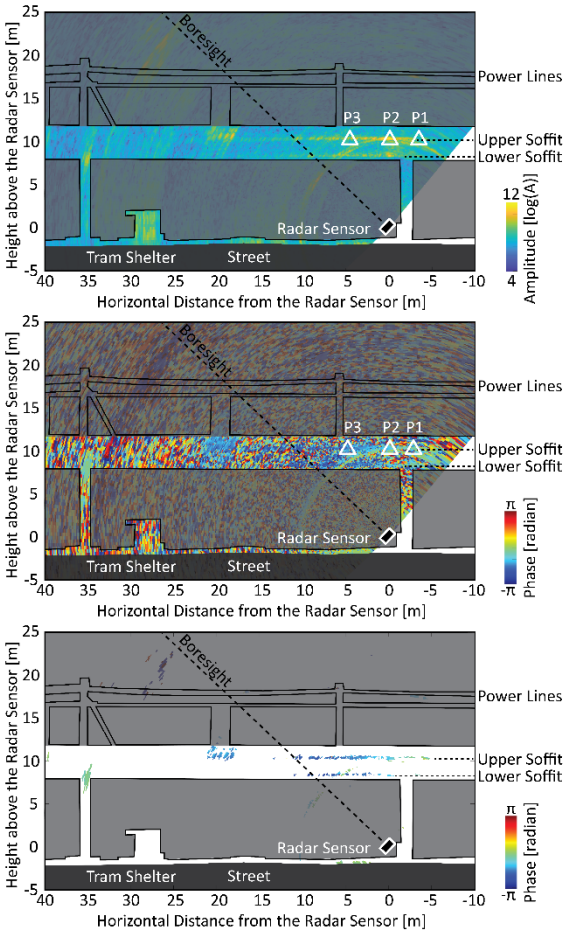

Figure 10. Image of the interferometric amplitudes (top) and phases (centre) of radar instrument A for the bridge experiment, and the bins remaining after filtering (bottom). The images are overlayed with a mask highlighting the parts of the scene visible (non-obstructed) for the instruments.

An example of an unfiltered interferometric phase image can be seen in Figure 10 (centre). This interferogram was computed from two SLCs gathered 148 seconds apart, one of them during an unloaded state and one while a train passed over the bridge. The interferogram mostly consists of random noise, because much of the scene shown in the figure is either empty space (air, not reflecting the radar signal sufficiently) or obstructed (the radar signals do not penetrate the pillars, bridge deck and other solid objects). Upon closer inspection, some small areas with little noise can be seen, e.g. a circular area at a distance of about 10 m. The same area stands out also in the amplitude image. The circle intersects with the upper soffit of the bridge; the radar signals are strongly reflected there because of the orthogonal LOS and the planar concrete surface. The circular area is a sidelobe caused by the impact of the particularly strong reflection at point P2 and the synthetic aperture data processing for cross-range resolution.

Before analysing the interferograms, areas with low amplitude and thus high phase-noise need to be excluded. We do this herein by thresholding on coherence (≥0.9) after (Touzi *et al.*, 1999) and amplitude stability index (≥0.75) after (Ferretti *et al.*, 2001). The result of this selection process is a relatively small set of persistent scatterers (less than 1% or 1300 of the bins from the SLCs) which are shown in Figure 10 (bottom) as points with colour corresponding to phase change.

Looking at this filtered interferogram, we can now identify the areas represented well by the radar images. A comparison with Figure 8 shows that the upper and lower soffit with an angle of incidence of less than 45° are observable, the metallic platform at the bridge, and the upper corner of the bridge pier at 35 m. Considering the colours with dark blue indicating a displacement of π rad i.e., approximately 1 mm, towards the radar instrument and dark red 1 mm away, we notice a downwards displacement of the soffit and the metallic platform of roughly 0.5 mm with the train passing over the bridge. Little to no deformations is indicated at the locations of the two bridge piers at -2.5 and 35 m. These results are in accordance with the expected behaviour.

Spatial and temporal registering is required to compare or combine the acquisitions of both radar sensors. A coarse temporal registration was given by the timestamps of the computers used for data logging, and the registration was manually improved by shifting the timeseries of sensor B such that signals caused by trains passing occurred approximately simultaneously for both sensors. Better or automated temporal registration was not needed herein but could be achieved by cross-correlation using signals created by trains passing in both directions and on both tracks. The spatial registration was achieved by direct georeferencing of the radar sensors using geodetic measurements.

2022, Editorial Universitat Politècnica de València BY-NC-SA

C. *Results and analysis*

Ten trains passed over the bridge while the radar instruments were measuring. Figures 11 - 13 show the vertical displacements caused by a passing train driving on the track at the side of sensor A. The vertical displacements were calculated from the LOS displacements using Equation 3. The first figure shows the displacements-over-time for three selected bins (P1-P3, see Figures 8 and 10). For this graphic the time series have been down-sampled from 100 to 50 Hz for direct comparison with laser scanning observations (LS@P3) of P3, available from a different experiment (see Meyer *et al.*, 2022). P1 is located next to a bridge pier, and only small displacements are to be expected for this point.

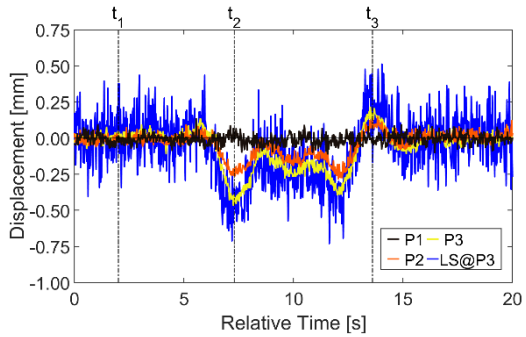

Figure 11. Displacement over time for three different positions along the bridge.

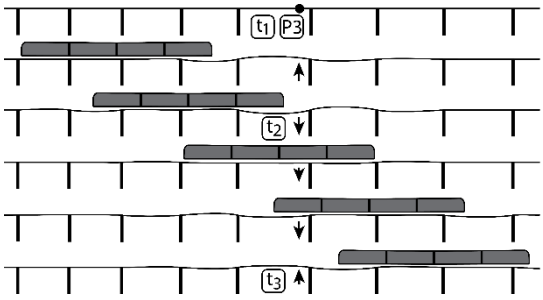

Figure 12. Deformation principle of the bridge with the example of a passing train. The arrows indicate the expected directions of deformation at P3.

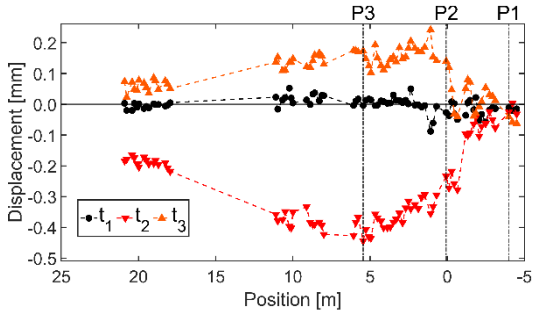

Figure 13. Displacement along the bridge as measured by instrument A for three different points in time.

Looking at Figure 11, we can see that no movements occur in the first five seconds of the time series. Afterwards, an approximately ten-second period with wave-like up- and downward movements occurs before the series stabilises again. The time series can be explained by the deformation expected with a train running over the bridge (see Figure 12, with t_1, t_2, and t_3 corresponding to the labels in Figure 11).

The laser scanner acquisitions are significantly noisier ($\sigma_{Vertical}$ = 152 µm) than the radar acquisitions ($\sigma_{Vertical}$ = 23 µm, both values are empirical standard deviations at P3 during a static period) but independently obtained with a different measurement principle and a slightly different viewing angle. The laser scanner was operated in profile mode with a temporal resolution of 0.02 s and an angular resolution of 0.08 mrad. The points acquired over a length of 5 cm along the profile were averaged and allowed calculating displacements of the area at point P3 also covered by the radar sensor and shown in Figure 11. Except for the noise levels the time series correspond to each other, and thus the laser scanning observations corroborate that the radar data yield the real surface displacements.

Looking at Figure 13, we see the deformation for bins located in parallel to the main axis of the bridge for t_1, t_2, and t_3. The bins are not uniformly distributed along the axis as can be seen in Figure 10(bottom). Furthermore, the bridge seems not to deform symmetrically but the pattern is reasonable because when extending the trend of deformation to the left, all three series intersect at about $+30$ metres which coincides with the next pier.

On another occasion, two trains in opposite directions passed almost simultaneously. Figure 14 shows the displacements of the bridge at location P3 as measured by instrument A and at the opposite side of the bridge as measured by instrument B. The first train passed on track T2 (see Figure 8) on the side of instrument B and did not cause a visible torsion. The second train on the opposite track T1 (see Figure 8) caused torsion. We have also observed this with other train passages: trains passing on track T1 always caused torsion, while trains passing on track T2 did not. This can be explained by the construction of the bridge. The observed section is part of a curved line and the bridge deck is slightly inclined. The shear center lies on the symmetry axis of the bridge (Figure 9). This means that the force exerted on the bridge by a train on the inner carriageway is directed towards the shear center and thus causes a uniform lowering. In contrast, a train on the outer carriageway causes torsion because the force is not directed in the direction of the shear center.

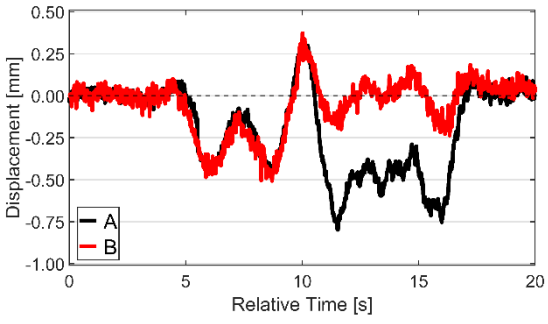

BY-NC-SA 2022, Editorial Universitat Politècnica de València

Figure 14. Displacement along the bridge as measured by instruments A and B for a cross section near P3.

V. Conclusion

Automotive-grade radar systems of type MIMO-SAR are potentially very useful for structural monitoring. They allow measuring surface displacements from distances of up to several tens of meters, with quasi-continuous areal coverage, temporal resolution of up to several hundred hertz and detection of displacements larger than about 0.02 mm. In this paper, we explored the feasibility of operating two identical MIMO-SAR systems simultaneously and thus increasing the spatial coverage.

We first investigated experimentally the impact of interference by carrying out measurements concurrently using two radar instruments operating in the same frequency band, once with full frequency overlap and once with non-overlapping frequencies. Since the available devices do not allow synchronization, we chose quasi-random interference patterns by using slightly different data acquisition rates and thus temporally varying degrees of interference covering all situations from 0 to 100% signal overlap. The results showed sporadic outliers or peak-like interference patterns overall only slightly affecting the precision of the displacement time series. While filtering those may be sufficient for monitoring slow movements, using disjoint frequency ranges is preferable for data acquisition if the high data rate of the radar instrument shall be exploited.

We then applied two MIMO-SAR systems with non-overlapping frequencies to monitor the vertical displacements of different parts of a railway bridge in response to passing trains. The sub-mm displacements were clearly delivered by the interferometric data processing and conversion from line-of-sight to vertical. The standard deviation of the individual displacements (per bin within the radar image) was on the order of 20 µm. The high-quality temporal and spatial deformation patterns provided contact-lessly by this low-cost measurement systems were checked for plausibility using the load situation and independent laser scans. The results corroborate the potential benefit of automotive-grade MIMO-SAR systems for structural monitoring, and the feasibility of operating such systems concurrently.

VI. Acknowledgements

We thank Tomislav Medic, Nicholas Meyer, Robert Presl, Lorenz Schmid, and Alexander Wolf, ETH Zurich, for support during the experiments and for providing the laser scanning results, as well as Eugenio Serantoni, Swiss Federal Railways (SBB), for comments on an earlier version of this paper.

References

Amar, R., Alaee-Kerahroodi, M., and Bahavani Shankar, M.R. (2021). FMCW-FMCW Interference Analysis in mm-Wave Radars; An indoor case study and validation by measurements. In: *21st International Radar Symposium (IRS)*, online, pp. 1-11.

Baumann-Ouyang, A., Butt, J.A., Salido-Monzú, D., and Wieser, A. (2021). MIMO-SAR Interferometric Measurements for Structural Monitoring: Accuracy and Limitations. *Remote Sensing*, Vol. 12, No. 21: 4290.

Caduff, R., Schlunegger, F., Kos, A., and Wiesmann, A. (2015). A review of terrestrial radar interferometry for measuring surface change in the geosciences, *Earth Surface Processes and Landforms*, Vol. 40, No. 2, pp. 208– 228.

Chae, B.-G., Park, H.-J., Catani, F., Simoni, A., and Berti, M. (2017). Landslide prediction, monitoring and early warning: a concise review of state-of-the-art. *Geoscience Journal*, Vol. 21, No. 6, pp. 1033-1070.

D'Aria, D., Falcone, P., Maggi, L., Cero, A., and Amoroso, G. (2019). MIMO Radar-Based System for Structural Health Monitoring and Geophysical Applications. *International Journal of Structural and Construction Engineering*, Vol. 13, No. 5, pp. 258-265.

Dham, V. (2020). Programming Chirp Parameters in TI Radar Devices. *Application Report SWRA553A*, Texas Instruments Inc., Dallas, TX, USA.

Enckell, M. (2011). Lessons Learned in Structural Health Monitoring of Bridges Using Advanced Sensor Technology. [Doctoral dissertation] KTH Royal Institute of Technology, Stockholm.

Ferretti, A., Prati, C., and Rocca, F. (2001). Permanent scatterers in SAR interferometry. *IEEE Transactions on Geoscience and Remote Sensing*, Vol. 39, No. 1, pp. 8-20.

Galmarini, A., Schmid, L., Ludin, M., and Wieser, A. (2020). Belastungsversuche zur Verifikation des Tragverhaltens. In: *20th Symposium Brückenbau*, Leipzig, Germany, pp. 114-119.

Holst, C., Kuhlmann, H., and Neuner, H. (2020). Analyse flächenhafter Schwingungen mit 3D-Laserscanning, In: *Beiträge zum 19. Internationalen Ingenieurvermessungskurs*, Munich, Germany, pp. 149-162.

Lienhart, W., Ehrhart, M., and Grick, M. (2017) High Frequent Total Station Measurements for the Monitoring of Bridge Vibrations. *Journal of Applied Geodesy*, Vol. 11, No. 1, pp. 1-8.

Meyer, N., Schmid, L., Wieser, A., and Medic, T. (2022). Vibration monitoring of a bridge using 2D profile laser scanning: Lessons learned from the comparison of two spatio-temporal processing strategies. In: *5th Joint International Symposium on Deformation Monitoring (JISDM)*, Valencia, Spain.

Miccinesi, L., Consumi, T., Beni, A., and Pieraccini, M. (2021). W-band MIMO GB-SAR for Bridge Testing/Monitoring. *Electronics*, Vol. 10, No. 18:2261.

Pieraccini, M., Miccinesi, L., and Rojhani, N. (2019). Monitoring of Vespucci bridge in Florence, Italy using a fast real aperture radar and a MIMO radar. In: *IGARSS 2019 – 2019 IEEE International Geoscience and Remote Sensing Symposium*, Yokohama, Japan, pp. 1982-1985.

Rao, S. (2018). MIMO Radar. *Application Report SWRA554A*, Texas Instruments Inc., Dallas, TX, USA.

Rödelsperger, S. (2011). Real-time processing of ground based synthetic aperture radar (GB-SAR) measurements.

2022, Editorial Universitat Politècnica de València (cc) BY-NC-SA

[Doctoral dissertation] Technische Universität Darmstadt, Darmstadt.

Rüeger, J.M. (2002). Refractive Index Formulae for Radio Waves. In: *Proceedings of the FIG XXII International Congress*, Washington, DC, USA, Vol. 113.

Sampaio, R.P.C., Maia, N.M.M., and Silva, J.M.M. (1999). Damage Detection using the Frequency-Response-Function Curvature Method. *Journal of Sound and Vibration*, Vol. 226, No. 5, pp. 1029-1042.

Scaioni, M., Marsella, M., Crosetto, M., Tornatore, V., and Wang, J. (2018). Geodetic and Remote-Sensing Sensors for Dam Deformation Monitoring. *Sensors*, Vol. 18, No. 11:3682.

Texas Instruments (2020). mmWave Radar Interface Control Document. Texas Instruments Inc. Dallas, TX, USA.

Tian, W., Li, Y., Hu, C., Li, Y., Wang, J., and Zeng, T. (2019). Vibration measurement method for artificial structure based on MIMO imaging radar. *IEEE Transactions on Aerospace and Electronic Systems*, Vol. 56, No. 1, pp. 749-760.

Touzi, R., Lopes, A., Bruniquel, J., and Vachon, P.W. (1999). Coherence estimation for SAR imagery. *IEEE Transactions on Geoscience and Remote Sensing*, Vol. 37, No. 1, pp. 135-149.

Yu, H., Lan, Y., Yuan, Z., Xu, J., and Lee, H. (2019). Phase Unwrapping in InSAR: A Review. *IEEE Geoscience and Remote Sensing Magazine*, Vol. 7, No. 1, pp. 40-58.

BY-NC-SA 2022, Editorial Universitat Politècnica de València